

Scanning magnetic tunnel junction microscope for high-resolution imaging of remanent magnetization fields

This content has been downloaded from IOPscience. Please scroll down to see the full text.

2014 Meas. Sci. Technol. 25 105401

(<http://iopscience.iop.org/0957-0233/25/10/105401>)

View [the table of contents for this issue](#), or go to the [journal homepage](#) for more

Download details:

IP Address: 136.152.142.6

This content was downloaded on 04/09/2014 at 22:26

Please note that [terms and conditions apply](#).

Scanning magnetic tunnel junction microscope for high-resolution imaging of remanent magnetization fields

E A Lima¹, A C Bruno², H R Carvalho^{2,3} and B P Weiss¹

¹ Department of Earth, Atmospheric and Planetary Sciences, Massachusetts Institute of Technology, Cambridge, MA 02139, USA

² Department of Physics, Pontifical Catholic University of Rio de Janeiro, Rio de Janeiro 22451-900, Brazil

E-mail: limaea@mit.edu

Received 12 April 2014, revised 11 June 2014

Accepted for publication 24 June 2014

Published 20 August 2014

Abstract

Scanning magnetic microscopy is a new methodology for mapping magnetic fields with high spatial resolution and field sensitivity. An important goal has been to develop high-performance instruments that do not require cryogenic technology due to its high cost, complexity, and limitation on sensor-to-sample distance. Here we report the development of a low-cost scanning magnetic microscope based on commercial room-temperature magnetic tunnel junction (MTJ) sensors that typically achieves spatial resolution better than $7\mu\text{m}$. By comparing different bias and detection schemes, optimal performance was obtained when biasing the MTJ sensor with a modulated current at 1.0 kHz in a Wheatstone bridge configuration while using a lock-in amplifier in conjunction with a low-noise custom-made preamplifier. A precision horizontal (x - y) scanning stage comprising two coupled nanopositioners controls the position of the sample and a linear actuator adjusts the sensor-to-sample distance. We obtained magnetic field sensitivities better than $150\text{ nT/Hz}^{1/2}$ between 0.1 and 10 Hz, which is a critical frequency range for scanning magnetic microscopy. This corresponds to a magnetic moment sensitivity of 10^{-14} A m^2 , a factor of 100 better than achievable with typical commercial superconducting moment magnetometers. It also represents an improvement in sensitivity by a factor between 10 and 30 compared to similar scanning MTJ microscopes based on conventional bias-detection schemes. To demonstrate the capabilities of the instrument, two polished thin sections of representative geological samples were scanned along with a synthetic sample containing magnetic microparticles. The instrument is usable for a diversity of applications that require mapping of samples at room temperature to preserve magnetic properties or viability, including paleomagnetism and rock magnetism, nondestructive evaluation of materials, and biological assays.

Keywords: scanning magnetic microscopy, magnetic tunnel junction sensors, rock magnetism, magnetic materials

(Some figures may appear in colour only in the online journal)

1. Introduction

Scanning magnetic microscopy for imaging room-temperature samples has attracted much interest in recent years owing to its potential to help elucidate a range of problems in science and

engineering involving imaging of magnetization and current distributions. Applications have spanned many disciplines, from applied physics and materials science [1–6] to paleomagnetism and rock magnetism [7–11], biophysics [12–20], and nondestructive testing [21–26]. Instruments based on superconducting quantum interference device (SQUID) sensors currently yield the best field sensitivity but are bulky,

³ Present address: Instituto Nacional de Metrologia, Qualidade e Tecnologia, Rio de Janeiro 25250-020, Brazil.

fragile, and very expensive to build and operate (particularly if low-critical-temperature SQUIDs are used for attaining maximal sensitivity). Furthermore, whereas many samples must be measured at room temperature to preserve their magnetic properties or viability, superconducting sensors must be maintained at very low temperatures (typically $<100\text{ K}$) inside a cryogenic vessel to sustain superconductivity. To overcome this hurdle, ingenious techniques have been devised to bring as close as possible two objects with such disparate temperatures [13, 27, 28]. Nevertheless, this difficulty has limited sensor-to-sample separations to no smaller than $80\text{--}100\text{ }\mu\text{m}$ for low-transition temperature SQUID microscopes. As a result of these difficulties, there has been an effort to develop alternative scanning magnetic microscopes that, while not as sensitive as scanning SQUID microscopes, may be easier to use, cheaper, and, perhaps most importantly, potentially achieve higher spatial resolutions.

Because of the rapid decay of magnetic fields with distance, an alternative approach for measuring weak magnetic moments is to use a sensor that, while perhaps having only modest field sensitivity, can be brought very close to the sample. As an example, the field of a magnetic dipole, which decays in intensity as the inverse distance cubed, measured $45\text{ }\mu\text{m}$ away from the source is about 10 times stronger than the field measured $100\text{ }\mu\text{m}$ away. Thus, a reduction in the sensor-to-sample distance by a factor of just 2.15 may yield up to a tenfold increase in field strength. Although not every source distribution produces magnetic fields that decay as rapidly as magnetic dipoles, significant gains in signal-to-noise ratio may be obtained by reducing the sensor-to-sample distance, particularly for specimens with heterogeneous magnetization.

Bringing the sensor closer to the sources can also improve spatial resolution, as long as other factors like sensor active area, thickness of the source distribution, and accuracy of the scanning stage do not impose additional limitations. The potential difficulties in reducing the sensor-to-sample distance are: the (i) increased effects of inconsistent sensor-to-sample distances encountered during scanning; (ii) strict mechanical accuracy and precision requirements on the scanning stage; (iii) risk of inducing spurious currents and magnetizations in the specimen; (iv) greater chance of damaging the sensor owing to friction and inadvertent collision with sample; (v) smaller scanning step sizes required for properly mapping a sample, leading to very long scans and reduced mapping areas; and (vi) introduction of artifacts into the field map associated with small mechanical vibration of the sensor.

Advances in thin-film deposition techniques and sensor miniaturization have enabled a diversity of noncryogenic sensor technologies for magnetic microscopy. Specifically, Hall-effect, giant magnetoresistance (GMR), giant magneto-impedance (GMI), and magnetic tunnel junction (MTJ) sensors offer a good cost-performance tradeoff [29–31]. MTJ sensors are especially attractive because of their relatively large field dynamic range, broad frequency response, bipolarity, small active area, and moderate cost. These sensors are based on the tunnel magnetoresistance (TMR) effect, in which electrons tunnel across a thin insulating layer sandwiched between two ferromagnetic metal films when a bias voltage

is applied across this ferromagnetic junction [32–34]. One of the ferromagnetic layers is pinned while the other is free to react to an applied magnetic field. The resistance of the device is a function of the applied magnetic field because the relative orientation of the magnetizations of the two ferromagnetic layers controls the tunneling current. The sensitivity and noise characteristics of MTJ sensors are generally superior to those of GMR and GMI devices [30], and special modulation and detection techniques can be employed to further improve their performance by reducing degradation of the signal-to-noise ratio by flicker ($1/f$) noise. Moreover, unlike other sensors, the MTJ device only requires a bias current of just a few tens of microamperes to operate, which is key for avoiding generating spurious magnetic fields that may induce currents and magnetizations in the sample. This is a critical issue that should not be overlooked when the sensor is placed closer than a few tens of micrometers away from a specimen. For instance, a 1 mA DC current—a lower bond for what is typically required to bias GMR and Hall-effect sensors—flowing on a $100\text{ }\mu\text{m}$ conducting structure situated $10\text{ }\mu\text{m}$ above a sample will generate a field of about $10\text{ }\mu\text{T}$ at the sample location, which is sufficient to induce perceptible magnetization components. MTJ sensors have traditionally used fixed background field structures to improve symmetrical field response, which may preclude accurate mapping of remanence in samples with low ratios of remanent magnetization to induced magnetization. However, newer MTJ designs are currently being developed to eliminate such structures [35]. Here we describe the development of a new scanning magnetic microscope based on commercial MTJ sensors optimized for high spatial resolution measurements of room-temperature samples. Our improvements represent a 10–30 fold increase in magnetic field sensitivity compared to that of similar instruments previously reported [1, 20].

2. Setup

We developed and tested the MTJ microscope at the Pontifical Catholic University of Rio de Janeiro (PUC-Rio) in Brazil (figure 1(a)). To reduce low-frequency interference from external sources typically found in an experimental laboratory (e.g. from the Earth's magnetic field, power lines, computers, and electronics in the same room), a two-layer mu-metal cylindrical magnetic shield was used to house the core components of the microscope: MTJ sensor, custom MTJ sensor preamplifier electronics, vertical positioning mechanism, and horizontal (x - y) scanning stage for sample displacement. The shield is 2.0 m high and 0.60 m in diameter (0.45 m inner layer diameter), and each layer comprises two mu-metal cylinders with access windows that can be closed or opened by rotating the outer cylinder in the corresponding layer. The access window in the outer layer is approximately $0.6\text{ m} \times 0.6\text{ m}$, whereas the inner layer has a $0.5\text{ m} \times 0.5\text{ m}$ opening. This shield was originally designed for housing the cryostat of a SQUID system, and smaller magnetic shields could be used for building a benchtop system provided that shielding factors greater than ~ 40 are obtained in the sensor region.

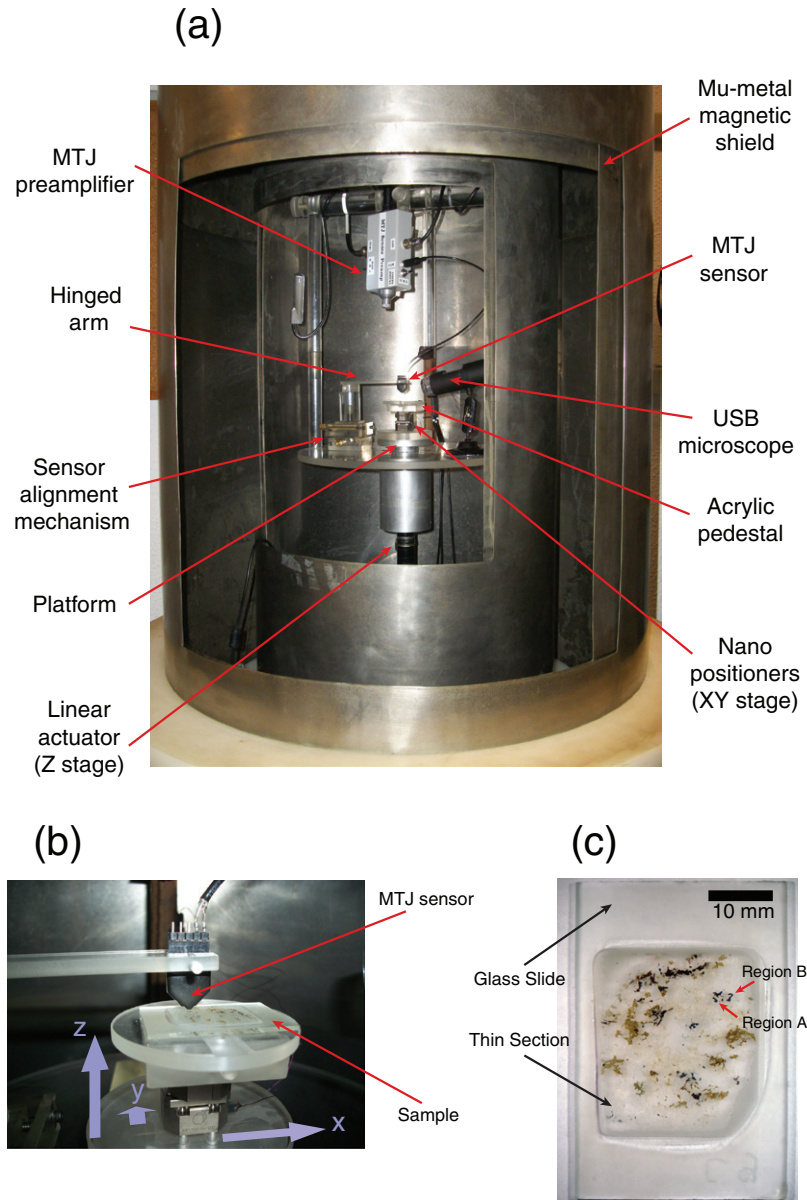


Figure 1. (a) Picture of the MTJ Microscope showing its various components. (The ancillary battery box is not visible in this picture.) (b) Detail showing (from bottom to top) nanopositioners, acrylic pedestal, sample (thin section), and MTJ sensor mounted to the hinged arm. Axes orientation is indicated by lavender-colored arrows. (c) Photograph of thin section of Vredefort granulite-gneiss showing the two regions that were mapped (figures 7 and 9).

Also located inside the shield is a universal serial bus (USB) optical microscope utilized for precisely adjusting the sensor's initial horizontal scan position by means of a manual sensor alignment mechanism. This optical microscope is also used to determine when the tip of the MTJ sensor touches the sample during the sensor-to-sample distance adjustment procedure. A small battery box (not shown) with three 9V alkaline batteries (or three 12V lead-acid rechargeable batteries for extended operation) provides clean DC power to the preamp to minimize AC power interference. The remaining components are situated outside of but in close proximity to the shield to minimize cable lengths and decrease noise pickup. This ancillary equipment, which consists of a commercial lock-in amplifier (Stanford Research Systems Model SR830) and a PC computer equipped with a USB digital

acquisition (DAQ) device, is used to demodulate and further amplify the sensor electronics' output signal and to record the magnetic signal while controlling the sample displacement. A custom LabVIEW program controls the scanning stage and the linear actuator and collects magnetic field data through the DAQ device. More details about the main components are described in the following.

2.1. MTJ sensor

We used MTJ sensors manufactured by Micro Magnetics, Inc. (models STJ-010 and STJ-020). Figure 1(b) shows a MTJ sensor mounted to the hinged arm during the scan of a polished rock thin section (figure 1(c)). The MTJ sensor die, which has an active area of about $4\mu\text{m} \times 2\mu\text{m}$, is located at the small tip

extending from a black protective epoxy layer. We used lapped sensors, for which the distance between the sensing area and the tip of the die is typically less than $10\mu\text{m}$. This configuration enables very small sensor-to-sample distances without compromising the robustness of the system. The device senses the magnetic field in a direction parallel to the die. Thus, if the sensor is mounted vertically, as in our microscope, the z -component of the magnetic field (i.e. normal to the scanning plane; see figure 1(b) for axes orientation) is measured.

Small sensor-to-sample distances not only improve the signal-to-noise ratio but are also critical for obtaining high-resolution magnetic field maps: the greater the separation between sensor and sample, the blurrier the field map, no matter which sensor is used to detect the magnetic field. To illustrate this point, consider the expression for the upward continuation of a potential field in a region of the space devoid of sources [36]. If $\vec{B}(x, y, h_0)$ is the vector magnetic field measured on the horizontal plane $z = h_0$, the field at a parallel plane $z = h_0 + \Delta h$ that is further away from the sources is given by

$$\vec{B}(x, y, h_0) * \psi(x, y, \Delta h), \quad (1)$$

where $*$ denotes a two-dimensional convolution performed for each field component separately, and $\psi(x, y, \Delta h) = (\Delta h / 2\pi) (1 / (x^2 + y^2 + \Delta h^2)^{3/2})$ is the upward continuation operator. Notice that ψ is essentially a single-peaked function that becomes more extended in the x and y directions as Δh increases. Therefore, a field map made at a sensor-to-sample distance $h_0 + \Delta h$ will always be a blurred version of the field map at h_0 because of the convolution operation with a broader ψ .

In particular, if all sources in a planar distribution lie at or immediately below $z = 0$ and we take $h_0 = 0$, then ψ approaches a two-dimensional Dirac's delta (i.e. infinite spatial resolution) as the sensor-to-sample distance Δh tends to zero.

The size of the active area of the magnetic sensor may also negatively impact spatial resolution in scanning magnetic microscopy owing to integration/averaging effects. However, in the case of our MTJ system, the sensor dimensions are two to three times smaller than typical sensor-to-sample distances, so that such effects may be neglected at first approximation. In general, the effective spatial resolution achievable with a scanning magnetic microscope is a complex issue and involves different factors in addition to the ones mentioned above, such as thickness of the magnetization distribution, map discretization (i.e. scanning step size), and positioning accuracy.

2.2. Scanning stage

Given the very small sensor-to-sample distances achievable with lapped MTJ sensors, it is critical for the scanning stage to have submicrometer precision and accuracy for displacing the sample horizontally while recording magnetic maps. Imprecision in the positioning of the sample relative to the sensor—the so-called position noise—is particularly important, as it is an effective noise source in the field map [37]. Another issue is the magnetic

field generated by the stage itself. This field may not only be picked up by the MTJ sensor, but could also induce a contaminating magnetization in the sample. We have employed a pedestal made of nonmagnetic material to increase the distance of the sample and sensor from the scanning stage.

In our microscope, two independent nanopositioners made of titanium (Attocube Systems, model ANPx100) were stacked and oriented perpendicularly, making up an x - y stage with a maximum travel of 5 mm in each direction. An acrylic pedestal is fixed to the stage, providing a flat surface for the sample to be mounted to and a 5 mm standoff separation to minimize spurious inductive effects. The positioners were controlled by electronics purchased from the same manufacturer (model ANC150/3). The x - y stage is mounted on a small aluminum platform that can be raised or lowered using a linear actuator (Zaber Technologies, model T-LA60A), allowing for the adjustment of the sensor-to-sample distance with micrometer accuracy. When scanning a sample, one of the axes moves continuously between the limits of the scanning area in that direction, whereas the other axis moves in discrete steps as each scan line is completed. Magnetic field values are acquired at regular time intervals determined by the prescribed step size and scanning speed. To ensure consistency of the step size, the DAQ device controls the timing of the acquisition by hardware. To avoid positioning mismatches owing to backlash and flexing of structures, data are only acquired when the scanning axis is moving in one direction, which yields submicrometer accuracy in the horizontal displacement of the sample.

Maximal spatial resolution and superior signal-to-noise ratio are achieved when scanning a flat polished sample with the sensor slightly touching the sample's top surface. In this configuration, although the $350\mu\text{m} \times 300\mu\text{m}$ sensor tip can withstand a small amount of roughness in the sample's surface, care should be taken to avoid scanning abrasive materials that could ultimately damage the silicon chip. Similarly, samples comprising soft materials could potentially get scratched by the sensor tip and therefore require careful setup. Nevertheless, by closely inspecting the samples prior to setting up scans we successfully mapped more than 20 different samples exceeding 100 magnetic field maps with a single MTJ sensor without experiencing any physical damage to the device or to the samples.

In addition to the scanning stage, an alignment mechanism displaces the sensor horizontally so as to allow for quickly centering the MTJ with respect to the region of interest within the sample, given that the travel range of the x - y stage is rather limited compared to the typical size of our samples. A hinged acrylic arm is attached to this mechanism and has a slot for fixing the MTJ sensor at its extremity. This arm exerts a small downward pressure to ensure consistent distance between the tip of the sensor and the surface of the sample when contact with the sample is desired.

2.3. Custom electronics

After performing initial tests using various commercially available electronics, we designed and built our own custom electronics to optimize the sensor biasing and signal detection scheme. By integrating all critical functions in a small,

shielded battery-powered circuit that is situated at close proximity to the MTJ sensor, we were able to significantly improve the sensitivity and overall performance of our instrument compared to what was achievable with commercial products (see section 3.1).

Because the MTJ response is bias-dependent [38], variations in the device's resistance due to applied magnetic fields might introduce small but undesirable nonlinear effects in the output voltage if the bias point is not properly fixed. To overcome this problem and achieve maximum linearity, we inject a current into a Wheatstone bridge instead of applying a voltage. We calculated the bridge parameters such that a virtually steady current is provided to the device. To decrease the low-frequency noise observed at the output of the MTJ sensor, we used a bias modulation scheme resembling the so-called "bias reversal" for SQUID sensors [39]. In this scheme, a square wave is used to modulate the bias current in combination with lock-in detection to extract small variations in the voltage signal measured across the Wheatstone bridge due to changes in the magnetic field detected by the MTJ sensor. While this is not strictly equivalent to modulating the source field to shift detection to a region of the spectrum with small $1/f$ and periodic noise components, it is rather effective in reducing low-frequency noise components typical of such sensors. The choice of bias frequency was carefully made to ensure a good compromise between cleanliness of the spectrum and responsivity of the MTJ sensor as a function of frequency. Because magnetic tunnel junctions exhibit capacitive effects [40] responsivity typically falls with frequency past a cutoff frequency, negatively impacting the signal-to-noise ratio.

The circuit of the MTJ sensor custom electronics (figure 2) is mounted on a four-layer printed circuit board using surface-mount devices for compactness and superior performance. It comprises five main blocks and is housed in an aluminum enclosure: (i) voltage regulation, (ii) clock generator, (iii) voltage-controlled precision current source (VCCS), (iv) Wheatstone bridge, and (v) differential amplifier. Three 9V batteries (alternatively, three 12V lead-acid rechargeable batteries that allow for longer operating cycles) are housed in a separate enclosure. The voltage regulation block provides four stable DC voltage levels: $\pm 6V$ (analog), $+5V$ (analog) and $+5V$ (digital). The majority of the circuit is powered by $\pm 6V$ with the exception of the clock generator and its associated optocoupler, which are powered by the $+5V$ and $+5V$ (digital), respectively. The digital power is completely isolated from the analog power using a separate battery and a separate voltage regulator.

The low-frequency clock generator provides an analog clock signal at a frequency adjustable through a potentiometer (1 kHz – 100 kHz). Because this chip requires $+5V$ DC to operate (which is too low for some of the other analog integrated circuits used) a separate voltage regulator supplies power to it. The output of the clock generator is split between the VCCS input and an optocoupler, which provides a transistor-transistor logic (TTL) sync out signal to trigger the lock-in amplifier. Alternatively, to accept an external clock signal, this block can be reconfigured using jumpers on the printed-circuit board (not shown in the schematic) by taking the sync

signal output from a lock-in amplifier and feeding it to the VCCS through the optocoupler.

The VCCS has a buffered trimming potentiometer at its input to adjust the basic bias current amplitude, I_0 . This scaled version of the analog clock signal is fed to a precision difference amplifier, which is the core of the current source. The output of the VCCS is connected to the two legs of the Wheatstone bridge. A switch allows for selecting modulated bias currents with amplitude I_0 , $I_0/2$, and $I_0/3$ by connecting different current-sensing resistors. We use bias currents ranging from $5\mu A$ to $30\mu A$, depending on the MTJ sensor characteristics.

The major purpose of the Wheatstone bridge is to remove most of the offset signal generated by the zero-field resistance of the MTJ sensor. By approximately balancing the two legs of the bridge, we are able to detect and amplify voltages associated with small variations in the MTJ resistance produced by weak magnetic fields in the vicinity of the sensor tip. The left leg of the bridge is comprised of two resistors R_b , which are >100 times larger than the MTJ resistance so that virtually all of the bias current flows through the opposite leg where the MTJ sensor is connected to. A reed relay is employed to short the two terminals of the MTJ sensor when turning the electronics on or off, so as to avoid voltage spikes that could potentially destroy the sensor. Also present in the right leg is a multi-turn potentiometer for balancing the bridge connected in series with one of three resistors (R_{s1} , R_{s2} , and R_{s3}), which is selectable by means of a switch. The purpose of these resistors is to accommodate MTJs with different nominal resistances. The values of these resistors are chosen to be slightly smaller than the nominal resistances of the sensors at hand so that the bridge can be approximately balanced by adjusting the potentiometer. The voltage between the two midpoints of the bridge is sensed by a differential amplifier.

The differential amplifier block is essentially a high input impedance instrumentation amplifier with selectable gain. Its aim is to amplify the (modulated) voltage signal proportional to the magnetic field in order to minimize degradation of the signal due to electromagnetic interference in the long cables connecting the circuit to the lock-in amplifier. A small capacitor is connected across the inputs of the instrumentation amplifier to help tame peaking that might otherwise occur due to the sharp transitions in the modulated bias current and the impedance imbalance between the two legs of the Wheatstone bridge. The amplified signal is then sent to the lock-in amplifier via the signal out connector.

The log-log plots of the responsivity curves measured for two MTJ sensors used in our instrument, hereafter denoted 'Sensor A' and 'Sensor B', show that the responses are flat until a few kHz, above which the performance starts to degrade (figure 3(a)). This behavior correlates with the impedance of such sensors, as seen in figure 3(b). The open circles represent measurements of magnitude and phase of the impedance of a MTJ device, which corresponds to 'Sensor B' shown in figure 3(a), whereas the solid lines show the fit of the theoretical model for the junction response [40] to the measured impedance data. We estimate

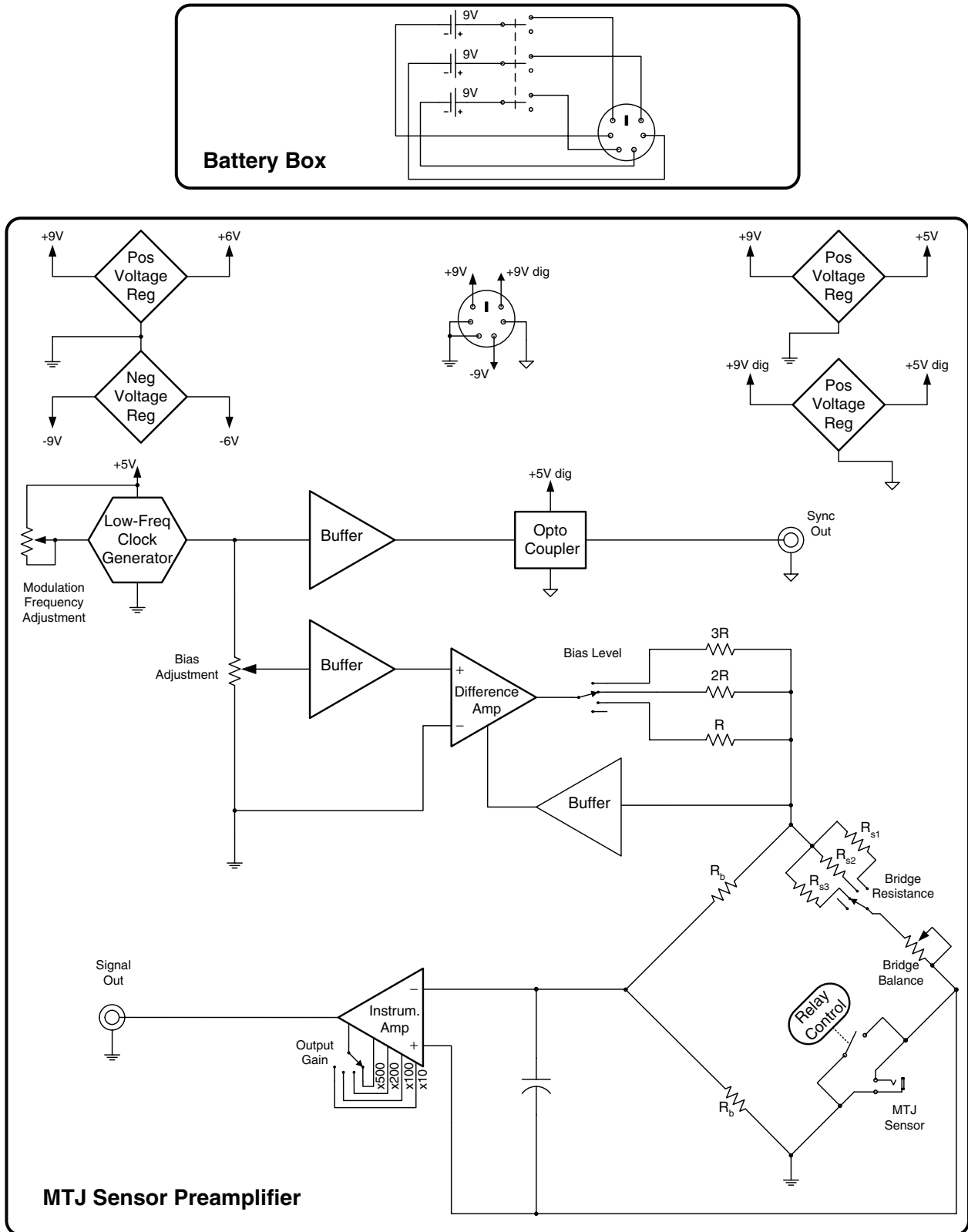


Figure 2. Schematic diagram of the MTJ sensor custom preamplifier circuit and ancillary battery box.

this sensor junction has an equivalent capacitance of 1.5 nF and an equivalent resistance of 9.5 k Ω . Based on such data and on repeated measurements of noise spectra up to 10 kHz on different days (data not shown), we chose a modulation frequency of 1 kHz.

3. Experimental results

We measured noise spectra and scanned synthetic samples to characterize the instrument's magnetic field sensitivity and spatial resolution. The main results are summarized in section 3.1.

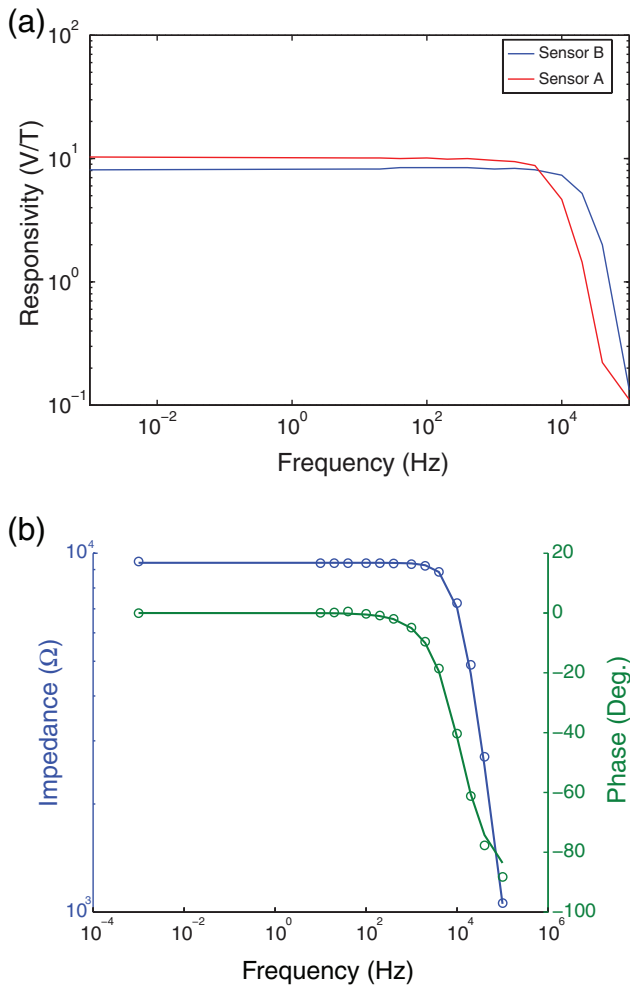


Figure 3. Sensor performance as a function of frequency. (a) Sensor responsivity as a function of bias modulation frequency. (b) Sensor impedance as a function of frequency (magnitude in blue, phase in green). Open circles denote measured values for Sensor B, whereas solid lines represent modeled values.

To demonstrate the performance of our instrument on actual samples, we scanned target areas in $30\mu\text{m}$ doubly polished thin sections representative of a metamorphic rock (figure 1(c)) and of an igneous rock (figure 8(a)), which are shown in section 3.2. For comparison, one of the thin sections was also mapped with the scanning SQUID microscope [13] in the MIT Paleomagnetism Laboratory. Also in section 3.2, we demonstrate how our MTJ microscope can be utilized as a vector magnetometer when measuring isolated features.

3.1. Performance characterization

To determine the sensitivity of our design, we compared noise spectra measured using three different setups under similar environmental conditions and with the cylindrical magnetic shield fully closed (figure 4). All measurements were performed using a commercial spectrum analyzer (Stanford Research Systems, model SR760) with AC input coupling (3 dB high-pass cut-off frequency of 0.16 Hz). The first spectrum, shown in blue in figure 4, was obtained with a commercial signal conditioning box

available from the manufacturer of the sensors (Micro Magnetics Inc. model AL-05). This box biases the sensor using a constant voltage. Even though the box is versatile and can be placed in close proximity to the MTJ sensor, it is powered by a switching DC power supply, which inevitably injects noise inside the shielded chamber through the output power cable.

We then replaced the AL-05 with a precision current source (Keithley Instruments model 6221) that generates a DC bias current together with a high-input-impedance low-noise differential preamplifier (Stanford Research Systems, model SR560) to measure the voltage across a discrete Wheatstone bridge similar to the one used in our custom electronics. The spectrum measured with this configuration is shown in black in figure 4. While the noise level above 3 Hz was smaller in this configuration, we observed a large increase in the component below 2 Hz. We attribute this increase to the long cables ($\sim 4\text{ m}$) used to connect the sensor inside the cylindrical shield to the preamplifier and current source located outside of the shield.

Finally, we measured the noise spectrum using our custom MTJ electronics (shown in red in figure 4). It is clear that the magnetic field sensitivity was improved by a factor of better than 20 compared to the setup using the AL-05 box over essentially all frequencies. The overall improvement over the spectrum measured with the benchtop current source and preamplifier was by a factor of 10 above 3 Hz, and several orders of magnitude at lower frequencies. The inset in figure 4 shows a detail of the noise spectrum measured with our custom electronics in the frequency range critical for scanning magnetic microscopy. (For the samples under consideration in this work, which produce static magnetic fields, spatial variations in the field are translated into time-varying signals by virtue of continuous sample displacement. The maximum frequency of the signal detected by the MTJ sensor is thus a function of the scanning speed, sensor-to-sample distance, sensor active area, and spatial distribution of magnetic sources. A 10 Hz bandwidth is large enough for scanning inhomogeneous samples with speeds below 1 mm/s at a sensor-to-sample distance of $\approx 7\mu\text{m}$.)

From these spectra, we can compute the magnetic moment sensitivity of our MTJ microscope by finding the magnetic dipole moment (Am^2) that produces a field at minimum sensor-to-sample distance with the same intensity as the peak-to-peak equivalent field noise [i.e. about 8x the root mean squared (RMS) field noise]:

$$m_{\min} = 4 \times 10^7 h^3 B_{\text{noise}} \text{ (SI units)}, \quad (2)$$

where h is the minimum sensor-to-sample distance achievable with the instrument and B_{noise} is the measured RMS value of the equivalent magnetic field noise in the frequency interval of interest. For a typical $7\mu\text{m}$ sensor-to-sample distance and a 10 Hz bandwidth, our MTJ microscope has a magnetic moment sensitivity of $\sim 10^{-14} \text{ Am}^2$, which corresponds to the $\approx 150 \text{ nT/Hz}^{1/2}$ magnetic field sensitivity shown in the inset of figure 4. For comparison, state-of-the-art commercially available superconducting rock magnetometers, which measure net moment without mapping fields, have sensitivities of 10^{-12} Am^2 . On the

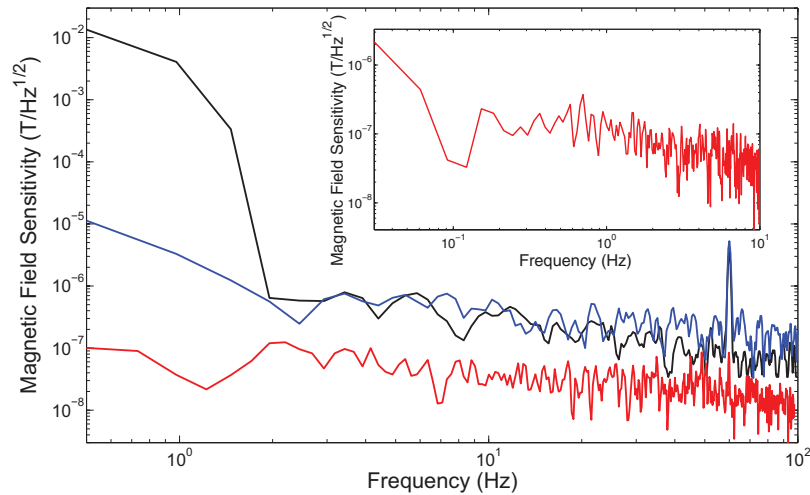


Figure 4. Comparison of noise spectra (RMS values, calibrated in field units) for three different bias-detection configurations: Micro Magnetics signal conditioning electronics AL-05 (blue trace), Stanford Research Systems low-noise preamplifier (black trace), and custom MTJ sensor electronics (red trace). Inset: detail of the custom electronics noise spectrum in the region below 10 Hz, which is the most critical for scanning magnetic microscopy.

other hand, our SQUID microscope has a magnetic moment sensitivity of $\sim 10^{-16}$ Am² at 100 μ m from the sample, which corresponds to a magnetic field sensitivity of ≈ 3 pT/Hz^{1/2} for frequencies below 10 Hz [13, 41]. Notice, however, that care should be taken when comparing the magnetic moment sensitivity values for the scanning magnetic microscopes because they are valid strictly for truly dipolar sources. In particular, at typical sensor-to-samples distances obtained with our MTJ microscope ($< 10 \mu$ m) only minuscule isolated sources behave as magnetic dipoles, which may require large underlying magnetizations to produce net moments of such strengths. This effect may lead to an additional difference in sensitivity for magnetization of up to 1 or 2 orders of magnitude.

The effective spatial resolution in scanning magnetic microscopy may be defined as the minimum distance between two magnetic point sources such that they are separated by 1 full width at half maximum (FWHM) of their single-peaked field maps without additional mathematical processing. We characterized our MTJ microscope's spatial resolution using measurements of the magnetic field of uniformly magnetized quasi-point sources. For an ideal point source like a magnetic dipole, a line scan performed directly over it will contain one or two distinct peaks whose characteristics can be used to infer the instrument spatial resolution and the sensor-to-sample distance. Because our MTJ microscope senses the z -component of the field (see figure 1(b) for axes orientation), it is convenient to measure point sources magnetized either in the $+z$ or $-z$ directions so that a single distinct peak is observed. By virtue of the blurring effect of the upward continuation operator (see section 2.1), the spatial resolution worsens as the sensor-to-sample distance increases. An estimate for the sensor-to-sample distance can be obtained directly from the FWHM measured for a point source (figure 5).

Whereas ideal point sources do not exist in practice, quasi-point sources can still provide very good estimates for the spatial resolution and for the sensor-to-sample distance. In this case, only upper limits on those quantities are obtained from measured FWHMs owing to the broadening of the peaks

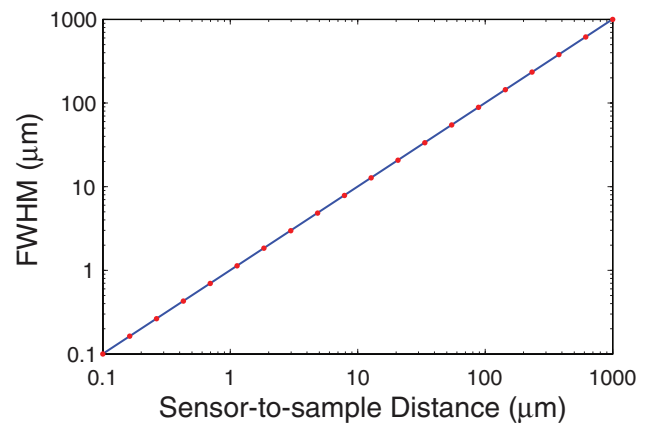


Figure 5. Full width at half maximum (FWHM) as a function of the distance between sensor and sample for a point source. The FWHM values (shown as red circles) were calculated from the simulated vertical (z) component of the magnetic field (i.e. component normal to the scanning plane—see figure 1(b) for axes orientation) of a magnetic dipole, oriented in the $+z$ direction, at various distances from the sensor. The blue trace represents the 1:1 line given by $\text{FWHM} = \text{sensor-to-sample distance}$.

associated with the integration of the magnetization over the source volume. We prepared a synthetic sample with magnetic microparticles to estimate the spatial resolution and the sensor-to-sample distance achieved with our scanning MTJ microscope. We sprinkled samarium-cobalt particles ($\text{Sm}_2\text{Co}_{17}$ alloy powder, average particle size of 10μ m) on a microscope glass slide coated with a thick layer of cyanoacrylate. After drying of the adhesive, the sample was gently sanded to reduce surface roughness and ensure that particles were flush with the top surface. Despite many particles having agglomerated in some regions of the slide, as expected, we also observed a number of isolated particles in the sample. Prior to mapping the sample, we imparted a strong isothermal remanent magnetization (IRM) by applying a short ≈ 0.5 T magnetic field pulse to the sample at room temperature with an electromagnet.

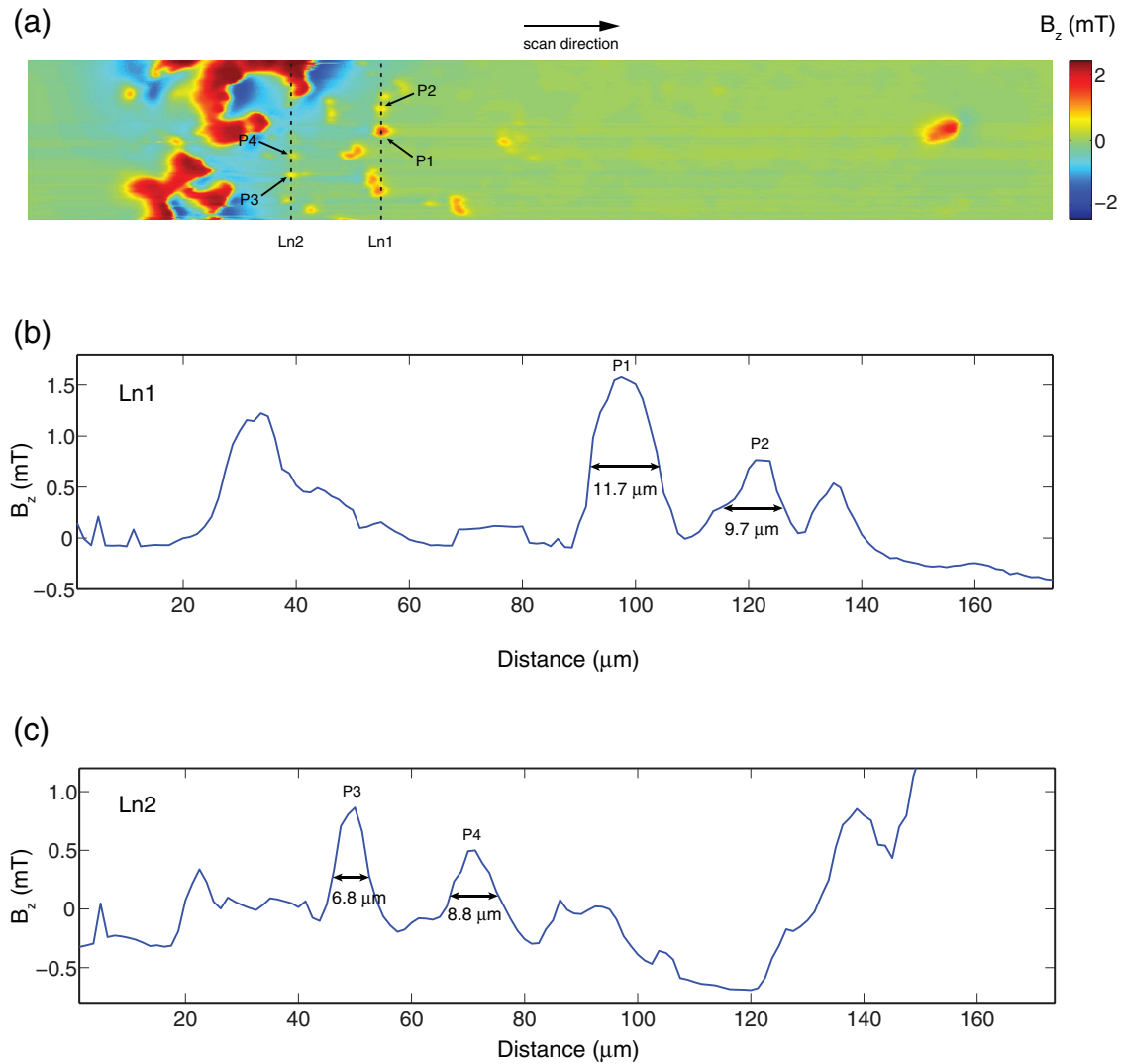


Figure 6. Magnetic field data from a synthetic sample utilized in the estimation of spatial resolution and sensor-to-sample distance. (a) Magnetic field map (z -component) of a 3.00 mm × 0.18 mm section of a synthetic sample comprised of $\text{Sm}_2\text{Co}_{17}$ microparticles attached to a glass microscope slide with cyanoacrylate adhesive. Four quasi-point sources (denoted P1, P2, P3, and P4, and indicated by black arrows) were selected for this analysis. Black dashed traces represent scan lines Ln1 and Ln2 passing through those sources. The color scale was slightly saturated to reveal weaker isolated sources in the sample. (b) Scan line Ln1 passing through P1 and P2, and corresponding FWHMs. (c) Scan line Ln2 passing through P3 and P4, and corresponding FWHMs.

We mapped the z -component of the magnetic field over a small region of the synthetic sample (figure 6(a)). Four isolated sources yielded measured FWHMs of 11.7, 9.7, 6.8, and 8.8 μm, respectively (figure 6(b), (c)). Such variations in measured FWHMs are in good agreement with the scatter of $\text{Sm}_2\text{Co}_{17}$ particle sizes in the powder used in the preparation of the synthetic sample (i.e. 10 μm average particle size and 9.3 μm average FWHM). Most importantly, the smallest measured FWHM shows that our spatial resolution is better than 6.8 μm, which is also an upper limit on the minimum sensor-to-sample distance achievable with our instrument.

3.2. Measurements of geological samples

We mapped two 30 μm thin sections of metamorphic and igneous rocks to demonstrate the capabilities of our MTJ microscope. We first scanned a sample from the 300 km

diameter Vredefort impact crater in South Africa [42]. The sample was prepared from a core drilled in granulite-gneiss within the 9 × 9 m² grid described in ref. [43]. Figure 7(a) shows a transmitted-light picture taken with an optical microscope of a small region of the thin section (denoted ‘region A’ in the full picture of the sample shown in figure 1(c)). The dark regions contain ferromagnetic minerals (mainly magnetite) that carry remanence, and are surrounded by nonmagnetic plagioclase feldspar and quartz. The inset shows a crossed-polars image highlighting the presence of a nonmagnetic feature, associated with dark bluish-gray silicate inclusions within the magnetite (white arrow). We imparted a strong-field IRM (0.4 T peak field) out of the sample plane prior to mapping to identify the spatial distribution of magnetic minerals and their relative capacity to acquire remanent magnetization. The map of the z -component of the field produced by the IRM at the minimum sensor-to-sample distance of ≈7 μm reveals

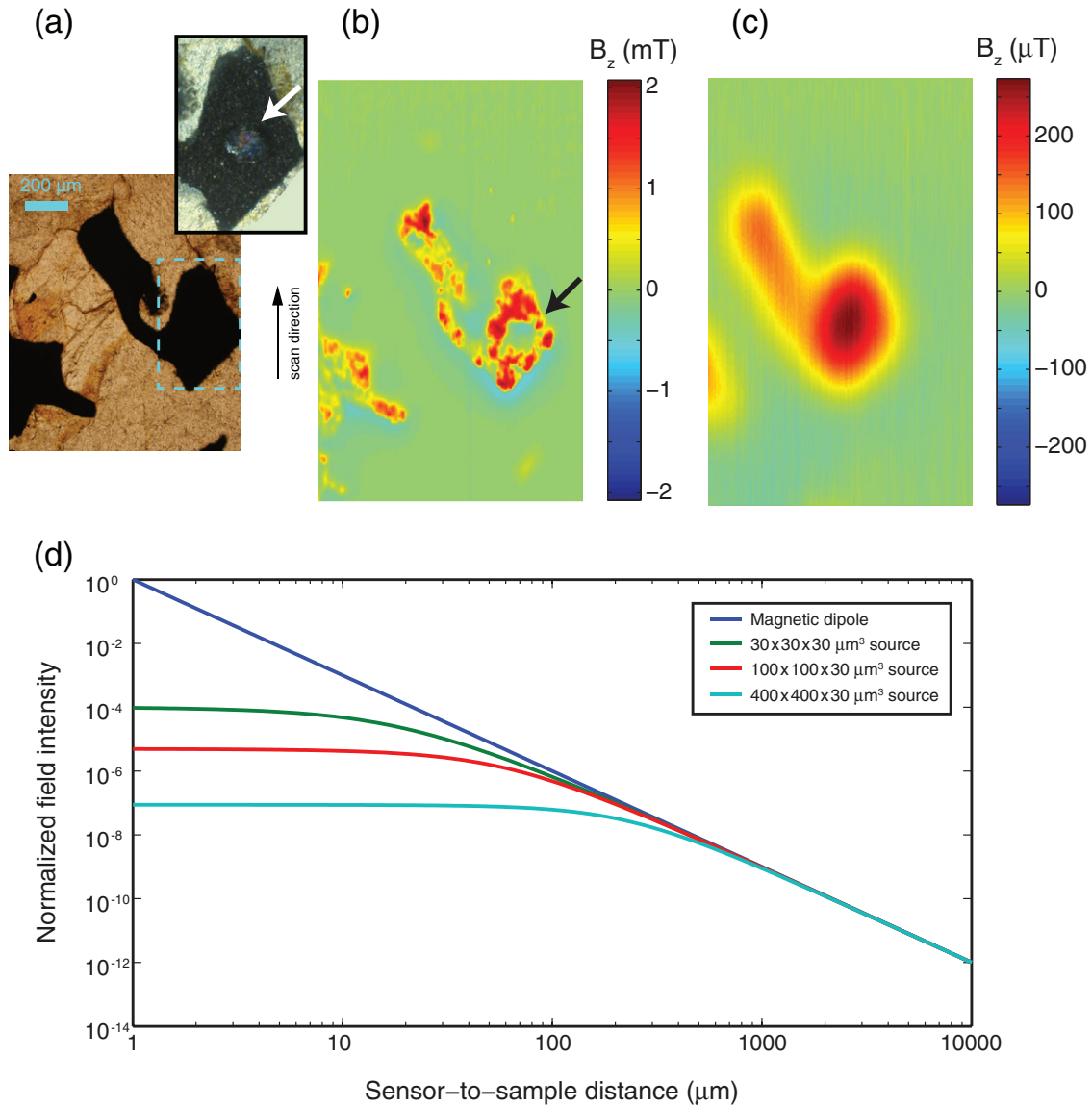


Figure 7. Small region in the thin section of granulite-gneiss from the Vredefort impact crater (labeled region A in figure 1(c)) and corresponding magnetic field maps measured at different sensor-to-sample distances with the MTJ microscope. (a) Transmitted-light microscopy image of the selected region. Dark features correspond to areas rich in magnetic minerals. Inset shows crossed-polars detailed image of the section indicated by a light blue dashed rectangle, where it is possible to see a nonmagnetic feature (white arrow) enclosed in magnetic minerals. (b) Map of the vertical component of the magnetic field of the sample measured with the MTJ sensor touching the sample (sensor-to-sample distance of $\approx 7 \mu\text{m}$). The black arrow indicates the area of the field map corresponding to the nonmagnetic feature shown in the inset in (a). (c) Map of the vertical component of the magnetic field measured over approximately the same region with the MTJ sensor $\approx 150 \mu\text{m}$ away from the sample surface. (d) Comparison of the spatial decay in magnetic field intensity for four simulated sources magnetized in the vertical (+z direction) and with identical net magnetic moments: (i) magnetic dipole (blue), (ii) $30 \times 30 \times 30 \mu\text{m}^3$ rectangular prism (green), (iii) $100 \times 100 \times 30 \mu\text{m}^3$ rectangular prism (red), and (iv) $400 \times 400 \times 30 \mu\text{m}^3$ rectangular prism (light blue). The magnetic dipole has constant $1/r^3$ field decay, whereas extended sources exhibit slower decay at sensor-to-sample distances smaller than the source size. (Field values were calculated directly above the sources.)

fine-scale in homogeneities in the underlying magnetization that are not readily visible on the optical image (figure 7(b)). We can also observe in this map that the plagioclase and quartz surrounding the magnetite are at least two orders of magnitude less magnetic, as expected for such minerals. Notice the region indicated by a black arrow, which corresponds to the nonmagnetic inclusions in the inset of figure 7(a).

To quantify the field decay of such extended sources and to emulate what a scanning SQUID microscopy map of the same region would resemble, we increased the sensor-to-sample

distance to $150 \mu\text{m}$ and mapped the sample again (figure 7(c)). In this case, the field intensity decreased by just a factor of ≈ 8 , despite a 22-fold increase in the sensor-to-sample distance. Given the inverse cubic dependence of dipolar fields on distance r , this small intensity decrease might seem surprisingly modest at first. The reasons for this are that (i) spatially extended sources produce fields that typically decay much less rapidly with distance than point sources and (ii) the magnetization distribution cannot be considered strictly planar (i.e. two-dimensional) in the first map because the sensor-to-sample

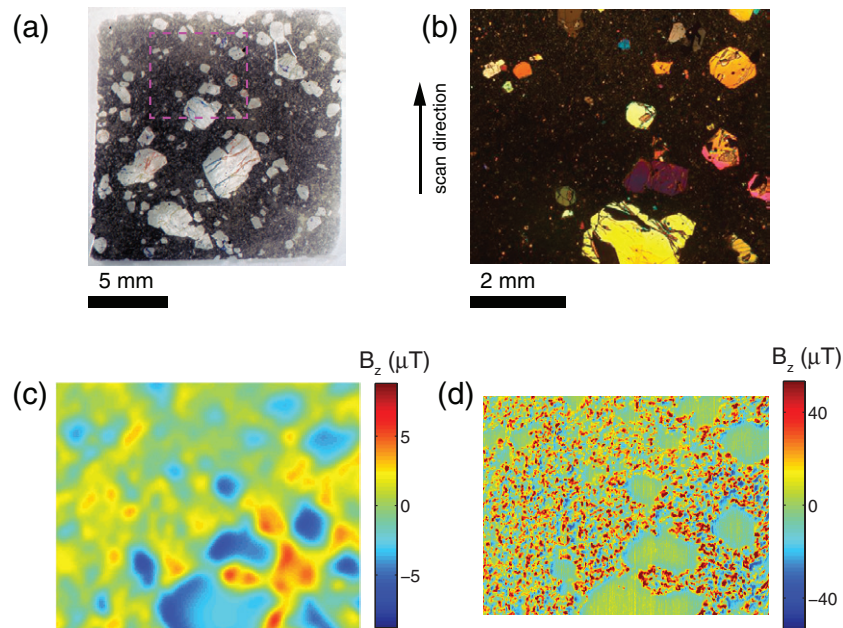


Figure 8. Thin section of a basaltic rock measured in a smaller region of interest both with the MIT SQUID microscope and with the MTJ microscope. (a) Reflected-light optical image of the $30\mu\text{m}$ polished thin section. The dark groundmass is rich in hematite and surrounds clear olivine phenocrysts of various sizes. Magenta dashed rectangle indicates the region that was mapped with the two scanning magnetic microscopes. (b) Crossed-polars transmitted-light microscopy image of the mapped region. Dark regions correspond to the groundmass, which is magnetic, whereas colored features are the nonmagnetic olivine phenocrysts. (c) Map of the vertical component of the magnetic field measured with the MIT scanning SQUID microscope at a sensor-to-sample distance of $\approx 190\mu\text{m}$. (d) Map of the vertical component of the magnetic field measured with the MTJ sensor touching the sample (sensor-to-sample distance of $\approx 7\mu\text{m}$) in the same target area of the thin section.

distance is less than a third of the sample thickness. If we take the average depth of the magnetization distribution into the calculation of the sensor-to-sample distance, the corresponding increase in sensor-to-sample distance is by a factor of ≈ 8 , and the field roughly decays as $1/r$ within this sensor-to-sample distance range. In fact, field decays slower than $1/r^3$ are expected for extended sources that are unidirectionally magnetized when measured at distances that are not much greater than the size of the distribution (figure 7(d)).

Notice that in the more distant field map (figure 7(c)), most details about the inhomogeneities in the magnetization distribution are lost and only the general shape is preserved. This may actually not be a detrimental effect in some studies. For instance, in paleomagnetism a large number of grains must be averaged to provide reliable records of ancient planetary magnetic fields preserved as remanent magnetization in rocks. Depending on the grain-size distribution of the minerals carrying the remanence, a map such as the one shown in figure 7(b) might be too detailed and figure 7(c) could offer a much better characterization of the sample for estimating the strength and direction of the paleofield. However, it is certainly beneficial to have the ability to map the field of a sample at a higher resolution to pinpoint regions containing good magnetic recorders.

The second sample analyzed was a thin section of olivine-phyric massive basalt sampled during the Hawai'i Scientific Drilling Project (HSDP2 [44]) through the Mauna Kea volcano (depth 1286 m, core box 413, and run 509) (figure 8(a)). This sample was also mapped with the MIT SQUID microscope

to provide a direct comparison between the spatial resolutions typically obtained with the scanning MTJ microscope and with the scanning SQUID microscope. The sample was imparted a 0.25 T IRM out of the sample plane (+z direction) prior to mapping so as to reveal the spatial distribution and relative strength of magnetic grains in the sample. The olivine phenocrysts appear as colored regions in the crossed-polars image of the thin section (figure 8(b)). The map of the z-component of the magnetic field of the sample in the target area measured with the MIT SQUID microscope at a sensor-to-sample distance exhibits a clear correlation with the petrographic image, with regions of negative field being associated with areas in the sample containing nonmagnetic features (figure 8(c)). These negative fields stem from the return field lines of the magnetized groundmass surrounding the olivine phenocrysts. Given that the dimensions of those features are comparable to the sensor-to-sample distance, such fringing fields advance well into the interior of the phenocrysts. Mapping the same region with the MTJ microscope at the minimum sensor-to-sample distance of $\approx 7\mu\text{m}$ revealed a magnetization distribution with very fine scale inhomogeneities (figure 8(d)). Here, we observe a strong correlation between the nonmagnetic olivine phenocrysts and areas in the field map with very weak field. In this case, the negative fringing fields are limited to the edges of the nonmagnetic features embedded in the groundmass owing to the reduced sensor-to-sample distance obtained with the MTJ.

Finally, we demonstrate how our MTJ microscope can be effectively utilized to obtain vector field maps of small samples and of specimens containing small isolated features.

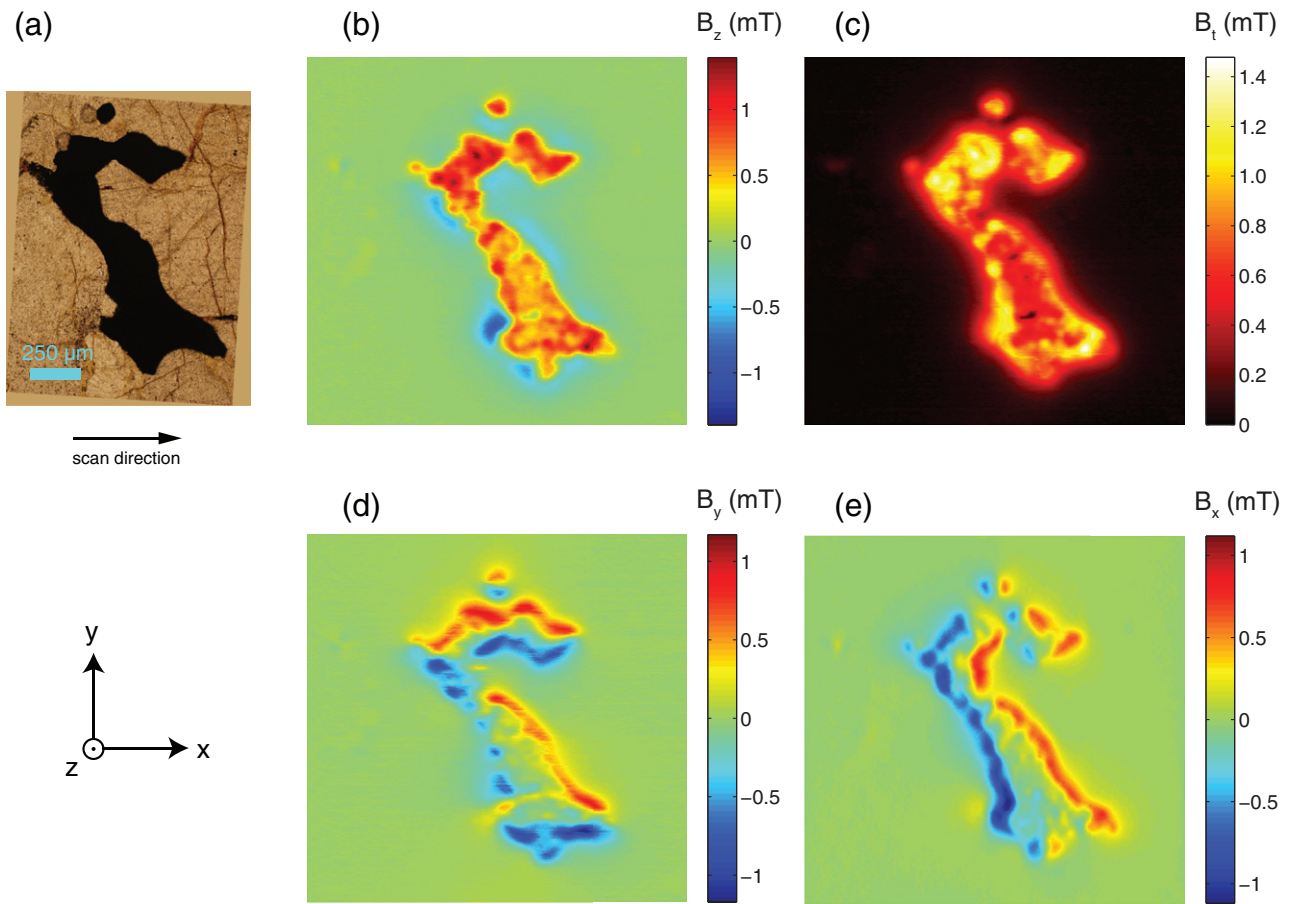


Figure 9. Small region in the thin section of granulite-gneiss from the Vredefort impact crater (labeled region B in figure 1(c)) and corresponding vector magnetic field maps estimated from the z -component map measured at a $\approx 7\mu\text{m}$ sensor-to-sample distances with the MTJ microscope. (a) Transmitted-light microscopy image of the magnetic feature. Dark areas correspond to zones rich in magnetic minerals. (b) Map of the vertical component of the magnetic field of the sample measured with the MTJ sensor touching the sample. (c) Map of the total magnetic field (i.e. field strength) estimated from the map shown in (b). (d) Map of the y -component of the magnetic field estimated from the map shown in (b). (e) Map of the x -component of the magnetic field estimated from the map shown in (b). Also shown in the figure is the orientation of the coordinate axes relative to the sample plane (see also figure 1(b)).

As discussed elsewhere [45], provided certain conditions are satisfied (e.g. near-zero field at the edges of the scanned area), maps of the x - and y -components of the field can be estimated from the map of the z -component. This technique does not depend on solving an inverse problem for the distribution of sources and it does not require that assumptions be made concerning the type of magnetic sources in the sample (e.g. current distributions vs. magnetizations).

Vector field maps are an invaluable tool in the interpretation of the magnetic field produced by complex magnetization and current distributions. Qualitative information regarding magnetization directions and spatial distribution of magnetic sources can be extracted from such vector maps and used to help selecting an adequate source model for the magnetic inverse problem to retrieve the underlying magnetization distribution from the measured field map. In general, the total field map carries information about regions devoid of sources, and roughly correlates with magnetization intensity, particularly for sensor-to-sample distances equal to or greater than feature sizes. On the other hand, the field component maps provide information regarding magnetization direction.

We illustrate this process of obtaining vector field maps from single-component measurements on the granulite-gneiss thin section by mapping a different region of the sample (region B in figure 1(c), shown in detail in figure 9(a)). In an area encompassing this region, we measured a map of the z -component of the magnetic field with the MTJ sensor touching the sample (figure 9(b), sensor-to-sample distance of $\approx 7\mu\text{m}$). Based on those data, we calculated the maps of the y -component of the field (figure 9(d)), x -component of the field (figure 9(e)), and then of the total field (figure 9(c)). It is clear that this sample has a unidirectional magnetization with perhaps a slight remanence anisotropy effect.

4. Conclusion

We built a scanning MTJ microscope with commercial MTJ sensors that utilize custom electronics. The instrument has magnetic field sensitivities better than $150\text{ nT/Hz}^{1/2}$ for frequencies below 10 Hz , which are the most critical for scanning magnetic microscopy. Proven sensor-to-sample separations better than $7\mu\text{m}$ were routinely achieved. The spatial resolution of our instrument for thin samples ($<10\mu\text{m}$ thickness),

at the minimum sensor-to-sample distance, is also $\approx 7\mu\text{m}$, as established by measurements of a synthetic sample containing regions with isolated magnetic microparticles. Such a spatial resolution is 14–30 times better than those typically obtained with scanning SQUID microscopes. However, the magnetic field sensitivity of the MTJ microscope is a factor of >10000 less than that of low-transition temperature SQUID microscopes. This sharp decrease in sensitivity is partly offset by the significant smaller sensor-to-sample distances achievable with the MTJ microscope, particularly for quasi-point sources whose fields decay very rapidly with distance. Specifically, the corresponding magnetic moment sensitivity for dipolar sources $7\mu\text{m}$ from the sensor and assuming a typical bandwidth of 10 Hz is $\sim 10^{-14} \text{ Am}^2$. In contrast, the magnetic moment sensitivity of our SQUID microscope is $\sim 10^{-16} \text{ Am}^2$ for dipolar sources located $100\mu\text{m}$ away from the sensor, while the moment sensitivity of a 2G Enterprises superconducting rock magnetometer is only 10^{-12} Am^2 . Our MTJ microscope therefore is a cost-effective complement due to its ability to map stronger fields [30] and higher spatial resolution compared to SQUID microscopy and due to its high sensitivity compared to SQUID moment magnetometry. We demonstrated the potential of our instrument to help analyze magnetic properties of rocks and magnetic materials in general at very fine ($<7\mu\text{m}$) microscopic spatial scales.

Acknowledgments

The authors would like to thank Laurent Carporzen for providing the Vredefort granulite-gneiss sample and Roger Fu for helpful discussions. We thank CNPq and FAPERJ for the financial support to develop the instrument and for providing travel funds for EAL, and the CNPq-MIT Cooperative Project and MIT-Brazil Seed Fund for providing travel funds for BPW and EAL. We also thank Mr Thomas F Peterson, Jr, for his generous gift to the MIT Paleomagnetism Laboratory in support of this research.

References

- [1] Volk M, Whitlock S, Wolff C H, Hall B V and Sidorov A I 2008 Scanning magnetoresistance microscopy of atom chips *Rev. Sci. Instrum.* **79** 023702
- [2] Yamamoto S Y and Schultz S 1996 Scanning magnetoresistance microscopy *Appl. Phys. Lett.* **69** 3263–5
- [3] Gregory J K, Bending S J and Sandhu A 2002 A scanning Hall probe microscope for large area magnetic imaging down to cryogenic temperatures *Rev. Sci. Instrum.* **73** 3515–9
- [4] Schrag B D and Xiao G 2003 Submicron electrical current density imaging of embedded microstructures *Appl. Phys. Lett.* **82** 3272–4
- [5] Schrag B D, Liu X Y, Shen W F and Xiao G 2004 Current density mapping and pinhole imaging in magnetic tunnel junctions via scanning magnetic microscopy *Appl. Phys. Lett.* **84** 2937–9
- [6] Lin W 2011 High resolution two-dimensional scanning magneto-resistive microscopy *PhD Dissertation* Carnegie Mellon University, Pittsburgh, PA
- [7] Egli R and Heller F 2000 High-resolution imaging using a high-T_c superconducting quantum interference device (SQUID) magnetometer *J. Geophys. Res.-Solid Earth* **105** 25709–27
- [8] Hankard F et al 2009 Magnetic field microscopy of rock samples using a giant magnetoresistance-based scanning magnetometer *Geochem. Geophys. Geosyst.* **10** Q10Y06
- [9] Kletetschka G et al 2013 Magnetic scanning and interpretation of paleomagnetic data from Prague Synform's volcanics *Studia Geophys. Geodaetica* **57** 103–17
- [10] Weiss B P, Lima E A, Fong L E and Baudenbacher F J 2007 Paleomagnetic analysis using SQUID microscopy *J. Geophys. Res.-Solid Earth* **112** B09105
- [11] Oda H et al 2011 Ultrafine-scale magnetostratigraphy of marine ferromanganese crust *Geology* **39** 227–30
- [12] Fong L E et al 2004 High-resolution imaging of cardiac biomagnetic fields using a low-transition-temperature superconducting quantum interference device microscope *Appl. Phys. Lett.* **84** 3190–2
- [13] Fong L E et al 2005 High-resolution room-temperature sample scanning superconducting quantum interference device microscope configurable for geological and biomagnetic applications *Rev. Sci. Instrum.* **76** 053703
- [14] Baudenbacher F et al 2005 Intracellular axial current in *Characorrallina* reflects the altered kinetics of ions in cytoplasm under the influence of light *Biophys. J.* **88** 690–7
- [15] Holzer J R, Fong L E, Sidorov V Y, Wikswo J P and Baudenbacher F 2004 High resolution magnetic images of planar wave fronts reveal bidomain properties of cardiac tissue *Biophys. J.* **87** 4326–32
- [16] Shen W, Schrag B D, Carter M J and Xiao G 2008 Quantitative detection of DNA labeled with magnetic nanoparticles using arrays of MgO-based magnetic tunnel junction sensors *Appl. Phys. Lett.* **93** 033903
- [17] Shen W et al 2008 Detection of DNA labeled with magnetic nanoparticles using MgO-based magnetic tunnel junction sensors *J. Appl. Phys.* **103** 07A306
- [18] Chemla Y R et al 2000 Ultrasensitive magnetic biosensor for homogeneous immunoassay *Proc. Natl Acad. Sci. USA* **97** 14268–72
- [19] Chan M-L, Jaramillo G, Hristova K R and Horsley D A 2011 Magnetic scanometric DNA microarray detection of methyl tertiary butyl ether degrading bacteria for environmental monitoring *Biosens. Bioelectron.* **26** 2060–6
- [20] Chan M-L, Jaramillo G, Son A, Hristova K R and Horsley D A 2009 Scanning magnetoresistance microscopy for imaging magnetically labeled DNA microarrays *IEEE Trans. Magn.* **45** 4816–20
- [21] Chatrathorn S, Fleet E F, Wellstood F C, Knauss L A and Eiles T M 2000 Scanning SQUID microscopy of integrated circuits *Appl. Phys. Lett.* **76** 2304–6
- [22] Matthews J, Wellstood F C and Weinstock H 2007 Fast NDE of superconducting magnet wires using a flow-through SQUID microscope *IEEE Trans. Appl. Supercond.* **17** 776–9
- [23] Isawa K et al 2010 Detecting degradation in Ni-based superalloy UDIMET 520 with scanning SQUID microscopy *Physica C* **470** 1529–33
- [24] Lee S Y, Viswanathan V, Huckans J, Matthews J and Wellstood F C 2005 NDE of defects in superconducting wires using SQUID microscopy *IEEE Trans. Appl. Supercond.* **15** 707–10
- [25] Lee T K, Morris J W, Lee S and Clarke J 2006 Detection of fatigue damage prior crack initiation with scanning squid microscopy *AIP Conf. Proc.* **820** 1378–85
- [26] Jaramillo G, Chan M-L, Milewski J O, Field R D and Horsley D A 2012 Ferrite scanning microscope based on magnetic tunnel junction sensor *IEEE Trans. Magn.* **48** 3677–80
- [27] Lee T S, Dantsker E and Clarke J 1996 High-transition temperature superconducting quantum interference device microscope *Rev. Sci. Instrum.* **67** 4208–15

- [28] Baudenbacher F, Peters N T and Wikswo J P 2002 High resolution low-temperature superconductivity superconducting quantum interference device microscope for imaging magnetic fields of samples at room temperatures *Rev. Sci. Instrum.* **73** 1247–54
- [29] Weiss R, Mattheis R and Reiss G 2013 Advanced giant magnetoresistance technology for measurement applications *Meas. Sci. Technol.* **24** 082001
- [30] Lenz J and Edelstein A S 2006 Magnetic sensors and their applications *IEEE Sensors J.* **6** 631–49
- [31] Persson A, Thornell G and Nguyen H 2011 Radiation tolerance of a spin-dependent tunnelling magnetometer for space applications *Meas. Sci. Technol.* **22** 045204.
- [32] Freitas P P, Ferreira R, Cardoso S and Cardoso F 2007 Magnetoresistive sensors *J. Phys.: Condens. Matter* **19** 165221
- [33] Moodera J S, Nassar J and Mathon G 1999 Spin-tunneling in ferromagnetic junctions *Annu. Rev. Mater. Sci.* **29** 381–432
- [34] Tsymbal E Y, Mryasov O N and LeClair P R 2003 Spin-dependent tunnelling in magnetic tunnel junctions *J. Phys.: Condens. Matter* **15** R109–42
- [35] Xiao G 2013 Personal communication, Micro Magnetics, Inc.
- [36] Blakely R J 1996 *Potential Theory in Gravity and Magnetic Applications* (New York: Cambridge University Press) p 441
- [37] Lee S-Y, Mathews J and Wellstood F C 2004 Position noise in scanning superconducting quantum interference device microscopy *Appl. Phys. Lett.* **84** 5001–3
- [38] Zhu T, Xiang X and Xiao J Q 2003 Bias dependence of tunneling magnetoresistance on ferromagnetic electrode thickness *Appl. Phys. Lett.* **82** 2676–8
- [39] Drung D and Mück M 2005 SQUID Electronics *The SQUID Handbook: Fundamentals and Technology of SQUIDS and SQUID Systems* vol 1, ed J Clarke and A I Braginski (Weinheim: Wiley-VCH) pp 127–395
- [40] Padhan P, LeClair P, Gupta A, Tsunekawa K and Djayaprawira D D 2007 Frequency-dependent magnetoresistance and magnetocapacitance properties of magnetic tunnel junctions with MgO tunnel barrier *Appl. Phys. Lett.* **90** 142105
- [41] Baudenbacher F, Fong L E, Holzer J R and Radparvar M 2003 Monolithic low-transition-temperature superconducting magnetometers for high resolution imaging magnetic fields of room temperature samples *Appl. Phys. Lett.* **82** 3487–9
- [42] Carporzen L, Gilder S A and Hart R J 2005 Palaeomagnetism of the Vredefort meteorite crater and implications for craters on Mars *Nature* **435** 198–201
- [43] Carporzen L, Weiss B P, Gilder S A, Pommier A and Hart R J 2012 Lightning remagnetization of the Vredefort impact crater: No evidence for impact-generated magnetic fields *J. Geophys. Res.-Planets* **117** E01007
- [44] Garcia M O, Haskins E H, Stolper E M and Baker M 2007 Stratigraphy of the Hawai'i Scientific Drilling Project core (HSDP2): Anatomy of a Hawaiian shield volcano *Geochem. Geophys. Geosyst.* **8** Q02G20
- [45] Lima E A and Weiss B P 2009 Obtaining vector magnetic field maps from single-component measurements of geological samples *J. Geophys. Res.-Solid Earth* **114** B06102